MICROFLUIDIC APPLICATIONS OF BUBBLE OSCILLATIONS INDUCED BY GEOMETRICAL CONSTRAINT

A thesis submitted to the University of Manchester
for the degree of Master of Philosophy
in the Faculty of Engineering and Physical Sciences

2014

Zuonaki Ongodiebi
School of Mathematics

Contents

List of Figures

The University of Manchester

Zuonaki Ongodiebi
Master of Philosophy
Microfluidic applications of bubble oscillations induced by geometrical constraint
December 15, 2014

We present an experimental study of the propagation of air finger/bubble through a fluid-filled microchannel with centered rectangular occlusion. The displacement of a wetting fluid (oil) by a non-wetting fluid (air) at a constant flow rate results in a family of steadily propagating fingers/bubbles analogous to the propagation modes recently reported by [15, 16, 17] in millimetre-scale tubes, indicating that gravity is not an essential physical mechanism that underpins the emergence of these states. The occurance of these propagation modes informed by a simple modification of the tube geometry revealed that models based on idealized pore geometries are not able to capture key features of complex practical flows. As the $Ca = \frac{\mu U}{\sigma}$ (which is the ratio of viscous to surface tension forces, where μ is the fluid viscosity, U is the velocity of the bubble and σ, the surface tension) increased beyond a given Ca_c, the bubbles either localized in the least-constricted regions of the cross section or exhibit spatial oscillations formed by periodic sideways motion of the interface at a fixed distance behind the moving finger tip. We found that the transition from symmetic to either localized or oscillatory state results from exchange of stability between two different states rather than a continous evolution from one state to another. Also, our experimental evidence suggests that the propagating fingers are dependent on the dimension of the channel and the obstacle. Our results reveal that air fingers and finite bubbles of aspect ratios $\alpha > 1$ (defined as $\alpha = L/W$ where L is the distance between the front and the rear of the bubble measured in its static symmetric state and W is the width of the bubble) exhibit propagation modes that are both quantitatively and qualitatively similar; but short bubbles with $\alpha < 1$ undergo a transition similar to that of a continous transition from one state to another. Our results conform with recent report of [34].

Declaration

No portion of the work referred to in this thesis has been submitted in support of an application for another degree or qualification of this or any other university or other institution of learning.

Copyright Statement

Acknowledgements

This study would not have been possible without the help of Professor Anne Juel for supervising and the Petroleum Technology Development Fund (PTDF) for funding. My sincere gratitude to all members of MCND for their encouragements and advice especially during weekly meetings. Special thanks to Dr. Alice B. Thompson and Dr. Andrew Hazel who had always been providing answers to my questions. Special thanks to Dr. and Mrs. S. A. Sanni, Dr. and Mrs Didi Essi and Dr. Promise, M. for their love and encouragement. Also, I would like to thank all my friends especially Emmanual, A., Binaebi, A., Adokiye, O., Raheem, M.A., Ayo, O., Peter, F., Ado, B. I. and family members for their love and care, especially to my lovely wife, Ebiere for her support, understanding and prayers. Above all, I give glory to God Almighty for the gift of life.

Chapter 1

1 Introduction

Understanding the flow of confined bubbles and droplets within natural and man-made channels reveal a wide range of industrial applications ranging from enhanced oil recovery to microfluidic chip-based chemical analysis. Microfluidics; which refers to a set of technologies used for controling the flow dynamics of very small amount of liquid and gases in a miniaturised system is an emerging research area not only due to reduced sample volumes and cost involved when compared with macro-sized components, but the ability to easily and accurately control the dynamics of the flow. In these systems, there is competition between interfacial, viscous and/or capillary forces. The study of viscous oil-water flows [29] and complex fluid flow [30] in microchannel at low Reyolds number are examples of viscous forces dominated flows while an experimental investigation of capillary instabilities in a microfluidic T-Junction by [31] analogous to the classical Plateau-Rayleigh instabilities is dominated by interfacial forces. Liquid-gas and liquid-liquid flows in microchannels have recieved increasing experimental research interests [1, 2]. Bubbly flow in microchannel have been shown to be very effective in heat transfer [5] and can effectively transport reagents and encapsulate cells to perform chemical reactions and biological experiments with high sensitivity [3, 4]. The ink-jet printing (a type of computer printing that creates a digital image by propelling droplets of ink onto paper, plastic or other substrates) is a product of an understanding of bubbles/droplets dynamics in confined geometries. Advances in digital microfluidics (an alternative technology for microfluidic systems based upon design, composition and manipulation of discrete droplets and bubbles) have facilitated the understanding of diverse and complex flow dynamics in microchannel network, as the formation, transport and merging of bubbles/droplets in microchannels are well understood [21]. Bubbles/droplets traveling

through microchannel has been successfully applied to encode and decode information and perform logical operations [22, 23]. Studies of two phase flows in microfluidic channel network with the introduction of bifurcations and loops have been shown to alter the flow behavior dramatically [22]. This is because a bubble/droplet arriving at a T-junction flows into the branch characterized by lower resistance to flow. The binary choice made by the droplets, causes flow resistance which influence the choice of subsequent droplets within the branch, thereby, modifying the liquid flow rates through the channels, provided the bubble/droplet does not break [24]. As droplets are produced, they are transported along the microfluidic channels by the carrier fluid thereby, displacing the fluid. For sufficiently small bubbles/droplets, this effect is not significant as they are passively advected by the carrier fluid. The displacement of one fluid by another immiscible fluid of lower viscosity (usually air) through a channel at fixed flow rate, results to the formation of long bubble (air finger) which significantly interacts with the channel geometry. This two-phase displacement flow is a fundamental fluid mechanics phenomenon such as the flow of oil and gas in oil pipelines, extraction of oil from porous media [6], mammalian breathing, biomechanics of the lungs [7], pulmonary airways [8] and emerging lab-on-chip technologies [12]. Many of such two-phase displacement studies have been performed in simple geometries such as rectangular and elliptical [9], polygonal [10] and circular cross-sections [11]. In these geometries, a family of steadily propagating air fingers is formed when air is introduced at a constant flow rate. These fingers are centered within the tube and are surrounded by a film of the viscous liquid. The film deposited at the walls of the capillary, which increases monotonically with the capillary number $Ca = \frac{\mu U}{\sigma}$ (which is the ratio of viscous to surface tension forces where μ is the fluid viscosity, U is the velocity of the bubble and σ, the surface tension), causes the bubble to move faster than the average speed of the fluid [12]. Further studies of the mechanics of pulmonary airway reopening was experimentally investigated by driving an air finger through a collapsed fluid filled elastic tube [26]. In most practical applications however, more complex geometries are involved. For example, the pores in carbonate oil reservoirs are irregular and consists of sudden changes in pore shapes and sizes [13]

and airway collapse or mucus build-up in the lungs [14].

Recently, [15, 16] introduced a centred partial occlusion in millimetric tubes of rectangular cross-section and uncovered multiple finger propagation modes when air is driven through a channel filled with viscous fluid. Similar study by [17] revealed that for sufficiently high occlusions, two alternative stable solutions are possible for low flow rates: a steadily propagating asymmetric air finger that spans the majority of the tube or a steadily propagating asymmetric air finger that localized within one of the side-channels. A two-dimensional numerical investigation of finger propagation modes captured all the finger dynamics earlier reported, and in addition, revealed a new mode of finger behaviour such as bifurcation associated with tip-splitting [18]. These recent findings of [15, 16, 17, 18] have shown that a change in pore geometry alters the dynamics of an air finger/bubble, indicating that models based on idealized pore geometries are not able to capture key features of complex practical flows, whose understanding is the motivation behind the present study.

In this study, we experimentally investigated and confirmed that the multiplicity of propagation modes uncovered in millimetric channels also exist in microchannels indicating that gravitational force does not dictate the physical mechanism that underpins the emergence of the multiple propagation modes. Furthermore, we extended the study to investigate the dymanics of finite (short) bubbles and determined the critical capillary numbers, above which transition takes place. Our microchannel geometry consists of rectangular cross-section with centered partial rectangular occlusion. These occlusions alter the flow properties by causing in-flow local resistance across the tubes.

The remainder of this dissertation will proceed as follows: In chapter 2, the governing equation describing two-phase (liquid-gas) flow is presented and a brief description of the Young-Laplace equation which explains the basis for bubble deformation in microchannels is highlighted. Also, we present some dimensionless numbers relevant to our experiments. Chapter 3 is focuses on local bifurcation theory such as Pitch-fork, Saddle node and Hopf bifurcations. In chapter 4, we discuss the experimental setup and give a detail description of our experimental procedures as well as the parameters used in our investigations. Also, we explain experimentally how the viscosity of a Newtonian fluid is determined. We describe the method of producing long and short bubbles and also give a detail procedure of the image processing technique adopted in analysing our images. Chapter 5 is concern with the presentation of results while the final chapter summarizes the major results of this dissertation.

Chapter 2

2 Two-Phase (Liquid/Gas) Flow Equations

This chapter presents the basic equations of the simultaneous flow of two fluid phases. As earlier stated, the two fluids are immiscible and there is no mass transfer between the phases. The liquid phase (e.g oil) is the wetting phase denoted by L while the non-wetting gas phase (e.g. air) is donated by G. We also include the concept of surface tension and the Young-Laplace equation as well as some dimensionless numbers that have significant effect on two-phase flows in microchannels.

2.1 Governing equations

The governing equations we considered in the present problem are the incompressible Navier-Stokes equations. The liquid and gas phases are written seperately as:

$$\rho_{_L}\left(\frac{\partial \mathbf{u}_{_L}}{\partial t} + \mathbf{u}_{_L}\cdot\nabla\mathbf{u}_{_L}\right) = -\nabla P_{_L} + \mu_{_L}\nabla^2\mathbf{u}_{_L} + \rho_{_L}\mathbf{g} \tag{2.1}$$

$$\nabla\cdot\mathbf{u}_{_L} = 0 \tag{2.2}$$

due to imcompressibility of the liquid phase and

$$\rho_{_G}\left(\frac{\partial \mathbf{u}_{_G}}{\partial t} + \mathbf{u}_{_G}\cdot\nabla\mathbf{u}_{_G}\right) = -\nabla P_{_G} + \mu_{_G}\nabla^2\mathbf{u}_{_G} + \rho_{_G}\mathbf{g} \tag{2.3}$$

$$\frac{\partial \rho_{_G}}{\partial t} + \nabla\cdot(\rho_{_G}\mathbf{u}_{_G}) = 0 \tag{2.4}$$

due to compressibility of the gaseous phase; where ρ_L is the density of the liquid phase, $P_{_L}$ is the liquid pressure, $\mathbf{u}_{_L}$ is the velocity of the liquid, $\mu_{_L}$ is the liquid viscosity and $\mathbf{g}$ is the gravity. Similarly, $\rho_{_G}$, $P_{_G}$, $\mathbf{u}_{_G}$ and $\mu_{_G}$ are respectively the density, pressure, the flow velocity of the gaseous phase and the viscosity of the gaseous phase. We

have that

$\nabla P_{_L} = -\rho_{_L}\mathbf{g} + \nabla P^*_{_L}$, $\nabla P_{_G} = -\rho_{_G}\mathbf{g} + \nabla P^*_{_G}$ which implies that

$\nabla P^*_{_G} - \rho_{_L}\mathbf{g} = \nabla P_{_G} - (\rho_{_L} - \rho_{_G})\mathbf{g}$ and $P^*_{_L}$, $P^*_{_G}$ represent the physical pressures in the liquid and gas phase respectively. We assumed no-slip condition at the tube walls. The kinematic boundary condition for the system is $\mathbf{R}_t \cdot \mathbf{n} = \mathbf{u} \cdot \mathbf{n}$ where $\mathbf{R}$ is the position of the interface and $\mathbf{n}$ is the normal vector at the boundary.

2.2 Surface Tension

Fluid molecules experience mutual attractive forces. In an event that this mutual molecular attraction is overcome via thermal agitation, the molecules transform from liquid phase to gaseous phase. For liquid-gas interface, the cohesive forces between the liquid molecules do not balance the attractive forces at the surface. Consequently, they cohere more strongly with neighbouring molecules at the surface, which tends to minimize the surface area; a phenomenon known as surface tension. Surface tension results to interesting and fascinating physical phenomena; such as droplets formation, formation of soap films and the formation of curved surfaces seen in a glass of water. Surface tension induces excess pressure inside a bubble which can be determined by the Young-Laplace equation. The Young-Laplace equation establishes the relationship between curvature, surface energy and pressure difference between two phases. It effectively describes both spherical and non-spherical bubble shapes either with or without the influence of external force. The general expression for the pressure difference between two phases seperated by non-spherical surface is

$$\triangle P = \sigma \left[\frac{1}{R_1} + \frac{1}{R_2} \right] \tag{2.5}$$

where $\triangle P$ is the pressure gradient, σ is the surface tension force, R_1 and R_2 are the radii of curvatures of phases 1 and 2 respectively. Equation (2.5) is the Young-Laplace equation. This equation is essential to bubble phenomena in microchannel.

Note: $\triangle P$ is positive and defined as the pressure at the convex side minus the pressure

at the concave.

In the absence of any external force, a static interface has the same mean curvature at every point. In large scale phenomena, such as ocean waves, $\triangle P$ due to surface tension is negligible as $R_1, R_2 \to \infty$. Conversely, for small scale phenomena, $\triangle P$ is significant as $R_1, R_2 \to 0$. In table 1, we present surface tension σ data for some liquid-vapour interface at different temperatures.

Liquid	$T(^oC)$	$\sigma(N/m)$
Water	20	0.073
Water	100	0.059
Blood	37	0.058
Mercury	20	0.47
Benzene	20	0.029
Glycerine	20	0.063
Galden HT 270	25	0.02
200cs Silicon oil	25	0.021

Table 1: Liquid-vapour interface surface tension values of some liquids at different temperatures

2.2.1 Magragoni Effect

Marangoni effect (or Gibbs-Marangoni effect) is the transfer of mass along an interface between two immiscible fluids propelled by surface tension gradient. The flow dynamics is directed from a region of low surface tension to a region of high surface tension. Surface tension gradient may be caused by temperature gradient, surfactants or electric charge surface potentials [32]. Some observable Marangoni effects are tears of wine, the stabilization of soap films, crystal growth e.t.c. Surfactants have strong effect on pressure drop which can push a bubble through a capillary.

2.3 Dimensionless number

Despite the fact that the assumption of the continuum hypothesis governs both macrofluidic and microfluidic flows, there exist some differences in the dimensionless numbers associated with large scale and that associated with small scale flows. In microchannels for instance, gravity does not affect the flow due to the small channel height. The resulting dimensionless Bond number: $B_o = \frac{\rho g h^2}{\sigma}$ (which is a measure of the relative importance of surface tension forces compared to body forces) is less than unity, and as a result, does not play significant role in microfluidic flows. Thus the orientation of the channels either vertical or horizontal has no influence on the flow regime. Also, the Reynolds number: $R_e = \frac{\rho U L}{\mu}$ (ratio of inertia to viscous forces, where U is the characteristic velocity change over the characteristic length scale L) for microchannel flows is usually small because the viscous effects are greater than the effects of inertia. At high numbers ($R_e \gg 1$), inertia is dominant and the momentum equation (2.1) reduces to Euler's equation describing ideal non-viscous flow. On the other hand, if ($R_e \ll 1$), equation (2.1) collapses to the creeping flow equation. Another important feature of the Reynolds number is that it characterizes whether the flow is laminar or turbulent. The Weber number: $W_e = \frac{\rho U^2 L}{\sigma}$ (a measure of the relative importance of the fluid's inertia compared to its surface tension) is small since surface tension plays dominant role in microfluidic flows. While the Reynolds, Bond and Weber numbers are small in microfluidic flows, the capillary number: $Ca = \frac{\mu U}{\sigma}$ (ratio of viscous to surface tension forces), can be either small or large depending on the flow rate Q. Finally, we introduce here a bulk measure of the fluid displacement referred to as Wet fraction $m = 1 - \frac{Q}{AU}$ (defined as the ratio of the liquid volume left behind when an air finger has exited the tube, to the total volume of the tube; where $A = WH - wh$ is the cross-sectional area of the tube). In our experiments, we used the wet fraction in the characterization of the flow dynamics of both air finger and finite bubbles; I must confess that we are yet to give a physical interpretation of m in the characterization of finite bubbles.

Chapter 3

3 Local Bifurcation Theory

The theory of bifurcation attempts to explain the numerous phenomena which occur in solids, in flows of liquid and gases when parameter values exceed a specific threshold. The buckling of the Euler rod, the onset of oscillations in an electric circuit and the different experimentally observed regimes in pipe flows both in large and small scales, all occur when a specific physical parameter exceeds a threshold value. In dynamical systems, when a small change in parameter values (or bifurcation parameter) results to sudden qualitative or topological behavioural change, bifurcation is said to have occurred in such a system. A central issue in the study of bifurcation in fluid mechanics is the characterization of the range of conditions above which certain flows exist as well as the mechanisms underlying the transitions between the different flow patterns. Bifurcation theory gives the mathematical existence of various bifurcation scenarios seen in experiments and other systems.

In this section, we introduce a local bifurcation theory such as symmetric breaking pitchfork bifurcation; a most fundamental bifurcation theory evident in two-phase displacement flow through an axially-uniform rectangular occlusion within a rectangular cross-section [15, 16, 17, 19, 34] as well as saddle node and Hopf bifurcations. We will adopt simpler equations in explaining these bifurcation theories in general. These simple (standard) equations are able to capture the different bifurcation types mentioned above.

3.1 Pitchfork Bifurcation

In this bifurcation, a family of fixed points transfers its stability traits to two families before or after the bifurcation point. The normal form is given as

$$\frac{du}{dt} = \mu u \pm u^3 \tag{3.1}$$

where $\mu \in \Re$ is a control parameter that can be externally tuned. If the transfer of stability occurs before the bifurcation points, it is called subcritical bifurcation ($\frac{du}{dt} = \mu u + u^3$) but if this takes place after the bifurcation point, it is referred to as supercritical bifurcation ($\frac{du}{dt} = \mu u - u^3$). Pitchfork bifurcations are inherent in physical systems that possess an underlying symmetry. (See figure 1). A typical example of Pitchfork bifurcation is the buckling of the Euler rod earlier mentioned.

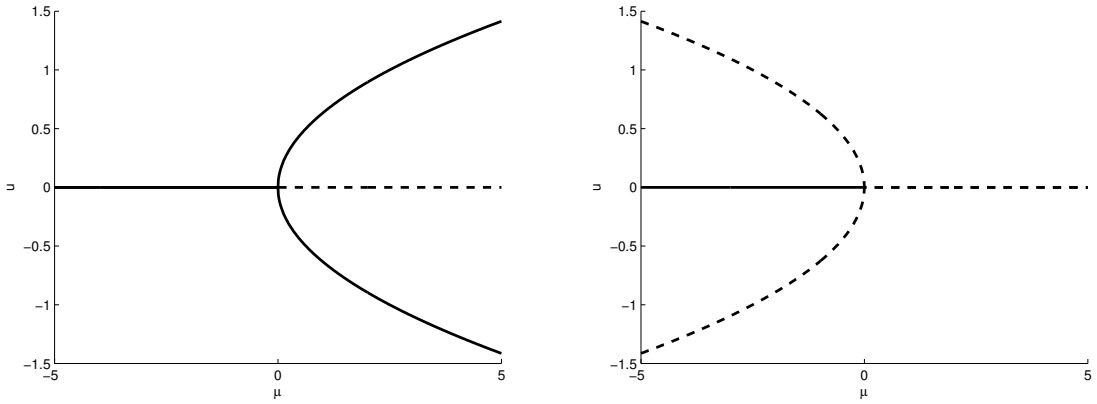

(a) (b)

Figure 1: (a) Supercritical and (b) Subcritical Pitchfork bifurcation. The solid line branches indicate stable solutions while the dash line branches denote unstable solutions.

3.2 Saddle-node Bifurcation

A saddle-node or turning point bifurcation results in a collision and subsequent disappearance of two equilibra positions in a dynamical system. The normal form is given by

$$\frac{du}{dt} = \mu \pm u^2 \tag{3.2}$$

The above equation can be written separately as $\frac{du}{dt} = \mu - u^2$ for supercriticality or $\frac{du}{dt} = \mu + u^2$ for subcriticality. In the supercritical case, the solution branch $u = \sqrt{\mu}$ is linearly stable while in the subcritical case, $u = -\sqrt{\mu}$ is the unstable solution branch. See figure 2

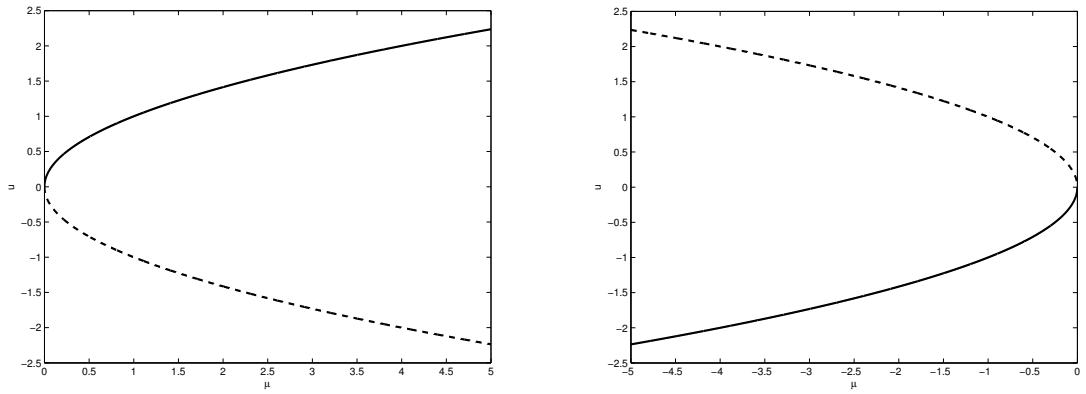

(a) (b)

Figure 2: (a) Supercritical and (b) Subcritical Saddle-node bifurcation. The solid line branches indicate stable solutions while the dash line branches denote unstable solutions.

3.3 Hopf Bifurcation

Hopf bifurcation (also called Poincaré-Andronov-Hopf bifurcation) is a bifurcation observed in form of local birth and death of a periodic solution as the parameter increases beyond a critical value. Hopf bifurcation occurs in differential equations when a linearised pair of complex conjugate eigenvalues at a fixed point becomes purely imaginary. This means that a Hopf bifurcation can occur in systems having two or more dimensions. The normal form of Hopf bifurcation when written in polar coordinates is given as

$$\frac{dr}{dt} = \nu r \pm r^3 \tag{3.3}$$

$$\dot{\theta} = \omega \tag{3.4}$$

As in Pitchfork bifurcation, the sign here also determined whether the Hopf bifurcation is subcritical or supercritical. See figure below

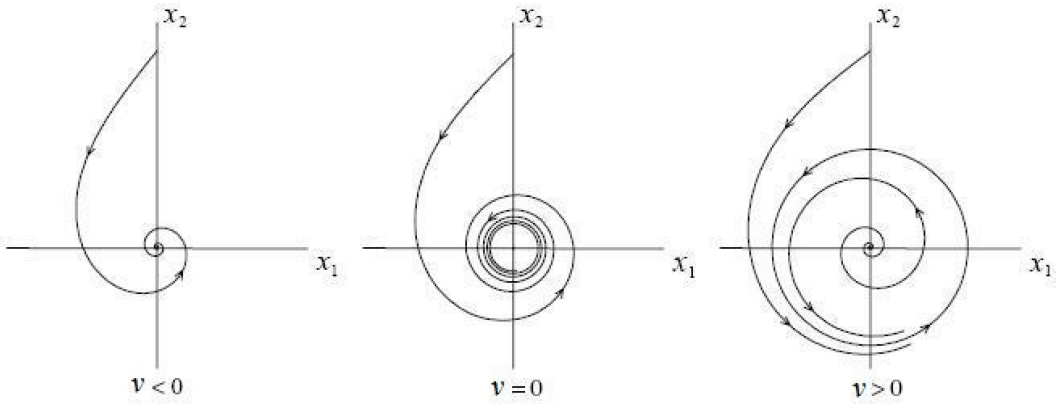

(a)

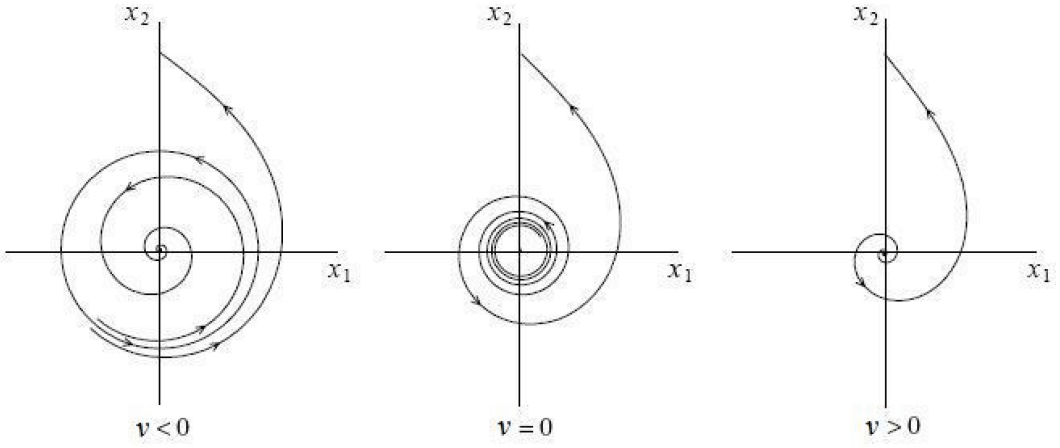

(b)

Figure 3: (a) Supercritical and (b) Subcritical Hopf bifurcation for parameter values: $\nu < 0$, $\nu = 0$ and $\nu > 0$ respectively. Source: [33]

Chapter 4

4 Experimental Methods

In this section, we present the experimetal setup and techniques developed to study the dynamics of long bubbles (air fingers) and short bubbles as they propagate through a fluid filled rectangular microchannel with centered partial rectangular occlusion driven by constant flux. The description of the experimental apparatus used for the study is given in §4.1. In §4.2, we present the properties of the fluid and describe the experimental procedure used to determine the dynamic viscosity. The process of producing long and short bubbles are discussed in §4.3 as well as the method applied to verify the uniformity of the channel. Finally, in §4.4, we present the imaging techniques with MATLAB image analysis toolsbox.

4.1 Experimental Setup

4.1.1 Description of the experimental apparatus.

The schematic channel diagram of the experimental setup is shown in figure 4. The channel was manufactured by micro-milling of a piece of perspex (CAT3D-M6, CNC, milling machine, Datron Technologies Ltd), and sealed with a clear adhesive film (Corning), which was supported by a precision-milled flat perspex lid. There are three channels labelled Channels 1, 2 and 3. The channels have constant height and length of 300 ± 5 μm and 9.60 ± 0.05 cm respectively with a rectangular centered partial occlusion each having constant length of 9.0 ± 0.05 cm thereby leaving a length of 0.60 ± 0.05 cm unoccluded space in all channel to allow initial states of the fingers/bubbles to be symmetric before driving them through the occluded part of the channels. The widths of both the channels and the obstacles were measured with a travelling microscope. The measurements were done at five regularly spaced locations along each channel and obstacle from which averaged values were determined

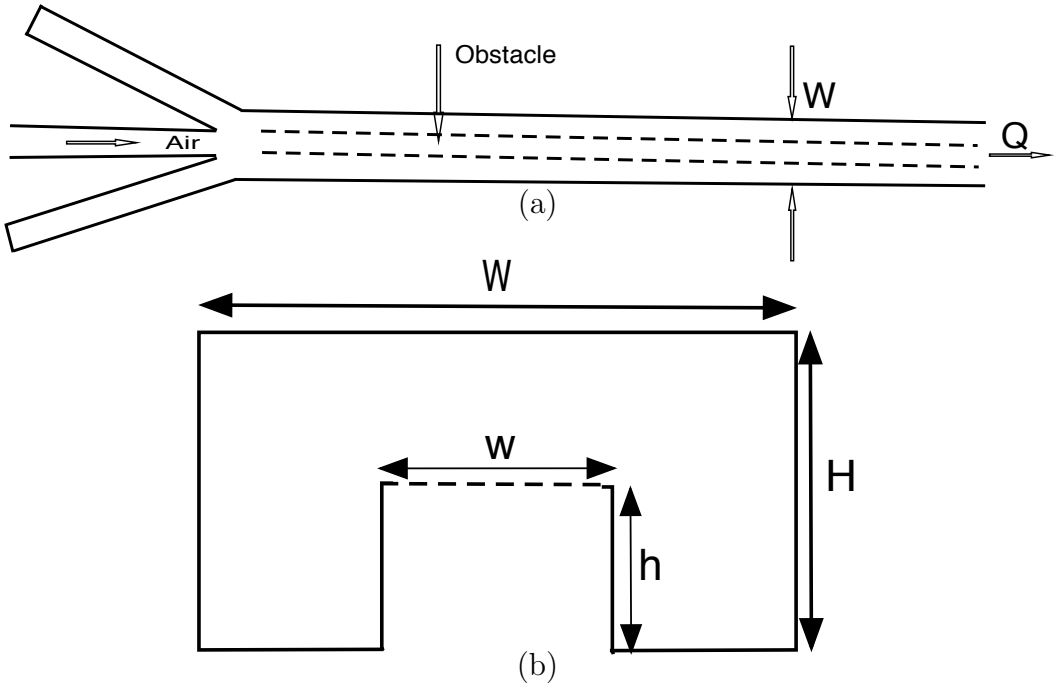

Figure 4: Schematic diagram of the channel geometry. Figure 4 (a) illustrates how liquid is withdrawn at constant flow rate Q from one end of the initially liquid-filled tube, with two of the outlets at the other end of the channel occluded for the production of an air finger while no outlet is occluded for the production of finite (short) bubble. Figure 4 (b) is the cross section of the channel. The outer width and height of the cross section are W and H respectively, while the corresponding centered rectangular occluded cross section are w and h respectively.

and shown in table 2. The specified depth values of both the channel and obstacle during production, are also presented in table 2. Each tube has three outlets at the beginning and an outlet at the rear. See figure 4 (a & b) for top and side views of the channel. The motion of the steadily propagating finger/bubble tips were recorded via top-view at a rate of 100 frames per second with high-speed (PCO) still camera with resolution (1280×1024) mounted on a 60 mm lens placed at a distance of 8.8 ± 0.05 cm above the microchannel. A LED light was difused through a sheet of tracing paper placed under the channel to capture the dynamics of the fingers/bubbles for different flow rates Q. These flow rates were produced with a syringe pump (KDS 210 KD scientific) connected to 500 μl syringe attached to the end of the channel through a flexible tubing. The velocity of the finger/bubble tip position U, between frames, and hence the capillary number Ca were determined from image analysis of the frames

with MATLAB. The aspect ratio of the channel; $\alpha = W/H$ (ratio of the width W and height H of the channel) lies in the range $1 \leq \alpha \leq 10$ typical of microfluidic channels [10].

Channels	$W \pm 5$ μm	$H \pm 5$ μm	$w \pm 5$ μm	$h \pm 5$ μm
Channel 1	1000	300	350	150
Channel 2	900	300	332	100
Channel 3	1000	300	333	150

Table 2: Channel and Obstacle dimensions. W and H denote the width and height of the channel while w and h represent the respective width and height of the obstacle.

4.2 Properties of fluid used

We used Galden HT 270 (Perfluorinated fluid from Solvay Solexis) for the experiment. Also, we used the manufacturer's specified surface tension value of 0.02 $Nm^{-}1$ at $25^{o}C$ in our calculations but we measured the viscosity and density of the fluid in our controlled laboratory temperature at $21 \pm 1^{o}C$ to be $\mu = 0.0313$ Pa.s and $\rho = 1856$ kg/m^3 respectively. We give detailed experimental process used to measure the viscosity here. The apparatus used were a capillary viscosmeter (size 5 & ref =65882 Poulten Selfe & Lee Ltd); (See figure 5), a stop watch, a clamp stand, and the fluid sample.

The viscometer was filled with the viscous fluid using tube (1), so that the sample is between (C & D). This will ensure that the amount of fluid does not obstruct Air Tube (2) during use. The viscometer was vertically positioned with a clamp stand to ensure accurate reading. A sealed rubber tubing was connected to (2) and a gentle suction was applied through (3) until the liquid reaches approximately 5mm above the upper timing (A). The liquid is held at this level by sealing tube (3). The air tube (2) was then released to allow the liquid to fall away from the bottom of the capillary tube. Finally, Timing Tube (3) is released to allow the liquid to flow under its own head. We measured the flow time in seconds for the bottom of the meniscus to pass from the top edge of (A) to the top edge of (B) with a stop watch. The process was repeated five times with $t = 577.874$ seconds as the averaged flow time. (Note: The measurement was done in the control laboratory temperature of $21^{o}C$).

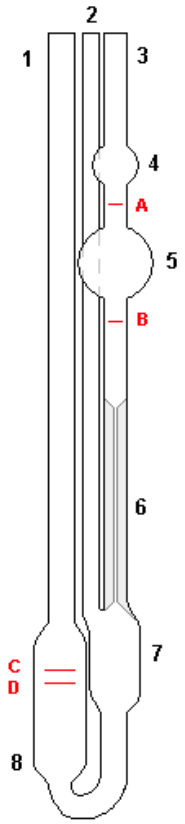

Figure 5: Ostwald viscometer

.

Now, kinematic viscosity is given as:

$$\nu = ct$$

where $c = 0.02739(\text{mm}^2/\text{s})/\text{s}$ is a constant value given by the manufacturer of the viscometer and t is the average time. Thus $\nu = 16.86814$ (mm^2/s) and the dynamic viscosity $\mu = \nu\rho = 0.0313$ Pa.s.

4.3 Production of finger & bubble

An air finger was produced by driving in air at a constant volume flux Q imposed by withdrawing the liquid at the end of the tube completely filled with viscous liquid with a syringe pump. After a short distance, the propagating finger advances at a constant speed. The finger is surrounded by a liquid film whose thickness increases monotonically with the capillary number. Finite bubbles were formed at the beginning of the unoccluded part of the channels with the three outlets open, by manually injecting air into the tube with a low constant flux flow. The air was injected with a 500 μl syringe and needle. We were able to produce different sizes of bubbles of unknown volumes, which we characterized by measuring their static symmetric length L (defined as the distance between the front and rear of the bubble). A short unoccluded rectangular inlet section ensured that the finger/bubble was initially symmetric about the mid-plane of the tube.

4.3.1 Uniformity of the Channels

The motion of a constant flux propagating finger/bubble is altered as it travels through wider or narrower sections of any channel. Thus we investigate the uniformity of the channels by driving in an air finger at low flow rate (Q=30 μl)/min through the channels. This is because at low flow rate, the finger is symmetric and fills the entire width of the channels with approximately zero contact angle (since the liquid fully wets the tube walls). The process was carried out both at the beginning (first half of length 4.5 ± 0.05 cm) and at the end (2nd half) of the three channels. This is so because the camera cannot cover the entire channel and still produced resolved images for experimental analyses. In figure 6, the front tip positions of the

bubble with respect to time both at the beginning and at the end of Channel 1 maintain an approximate speed of 1.46 mm/s. This shows that the channel is appreciably uniform along the entire length. Also, in Channels 2 and 3, the front tip positions of the bubbles with respect to time maintain approximate speeds of 1.51 mm/s and 1.46 mm/s respectively as the bubbles propagate the entire length of the channels as shown in figures 7 and 8. This indicates that the uniformity of the channels is ideal for experimental analyses.

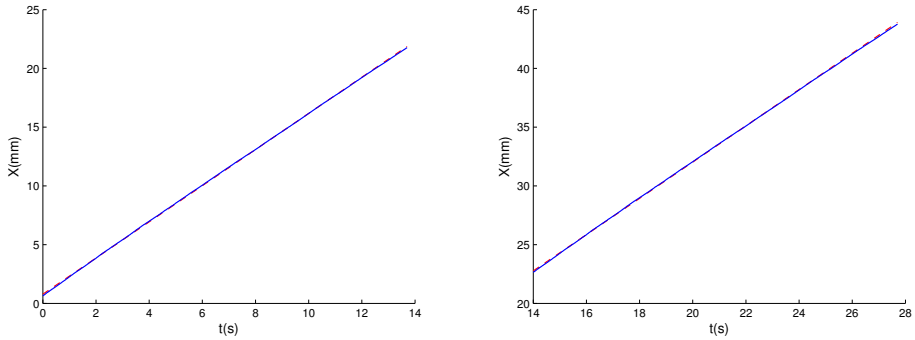

(a) beginning of channel (b) end of channel

Figure 6: Front tip oposition of long bubble as it propagates through channel 1. The speed of the bubble at the beginning of the channel was 1.46 mm/s and remained unchanged as it travels through the entire length of the channel. This is not unexpected since the graphs of figure 6 (a & b) are appreciably uniform along the entire channel.

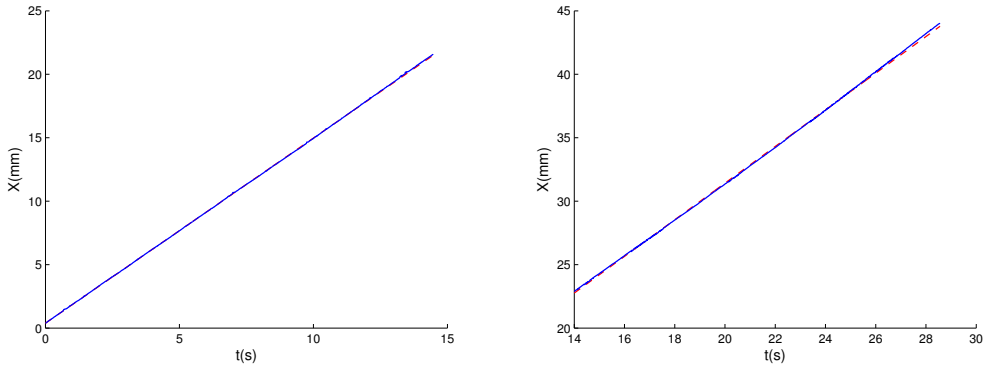

(a) beginning of channel (b) end of channel

Figure 7: Front tip position of long bubble as it propagates through channel 2. In this channel, the bubble maintains an approximate speed of 1.51 mm/s at the beginning and at the end of the channel.

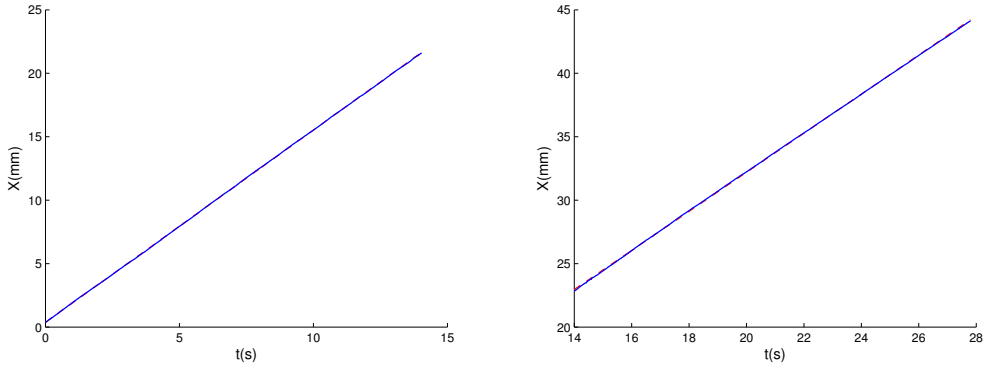

(a) beginning of channel (b) end of channel

Figure 8: Front tip position of long bubble as it propagates through channel 3. Also in this channel, the bubble maintains an approximate speed of 1.46 mm/s both at the beginning and at the end of the channel

.

4.4 Imaging process

Analyses of small scale two-phase displacement flows depend greatly on accurately detecting the visualized image edges of the displacement flow dynamics. Edge detection procedure was developed in Matlab in order to analyse the experimental images and to extract quantitative data of the flow dynamics. A built-in edge' fuction was used, which converts a captured video image, by detecting rapid changes in intensity, into a binary image, with the edges labelled as 1's and 0's for the background. The outer edges of the fingers/bubbles were visualized as dark contours due to the refraction at the air-oil interface of light through a tracing paper placed directly under the tube and viewed from above. The 'edge' function provides various edge detection methods and for this study, the 'canny' method was chosen. The 'canny' method enables the selection of two threshold values in order to detect both strong and weak edges. However, weak edges are only reflected in the output only if they are connected to strong edges. We were able to detect the visualized image edges and also their front tip positions as they propagate through the channel. The program was designed to extract all consecutive snapshots picturing the advancing tip position from each experimental movie (avi file). This enabled us to determine the average velocity of the finger/bubble as it propagates through the channel within the visualisation window. The algorithm is presented as follows:

(i) We read in the 'reference image' and also the image of an empty channel with 'imread' function in matlab and subtracted the image from the empty channel.

(ii) The region of view for both the subtracted and unsubtracted images were cropped before 'canny' edge detector was applied to detect the edges of the images by looking for local maxima of the image gradient. An 'image gradient' is a directional change in the intensity or colour of an image. The lower and upper thresholds were manually adjusted until a satisfactory threshold (threshold value which produces a clearer image edges) was achieved.

(iii) We then use the 'bwareaopen' function which removes from the binary images, all connected components (objects) that have fewer than 100 pixels and thereafter,

the binary images were closed with the 'imclose' function.
(iv) Furthermore, we used a flat linear structuring element with the 'strel' and 'bwconncomp' funtions to find the number of pixels in the region.
(v) Finally, the maximum pixels locations in the region and the coordinates are determined and plotted on the reference image.

The outputs of the matlab code are presented in figures (9 & 10) while the matlab code is given in appendix A.

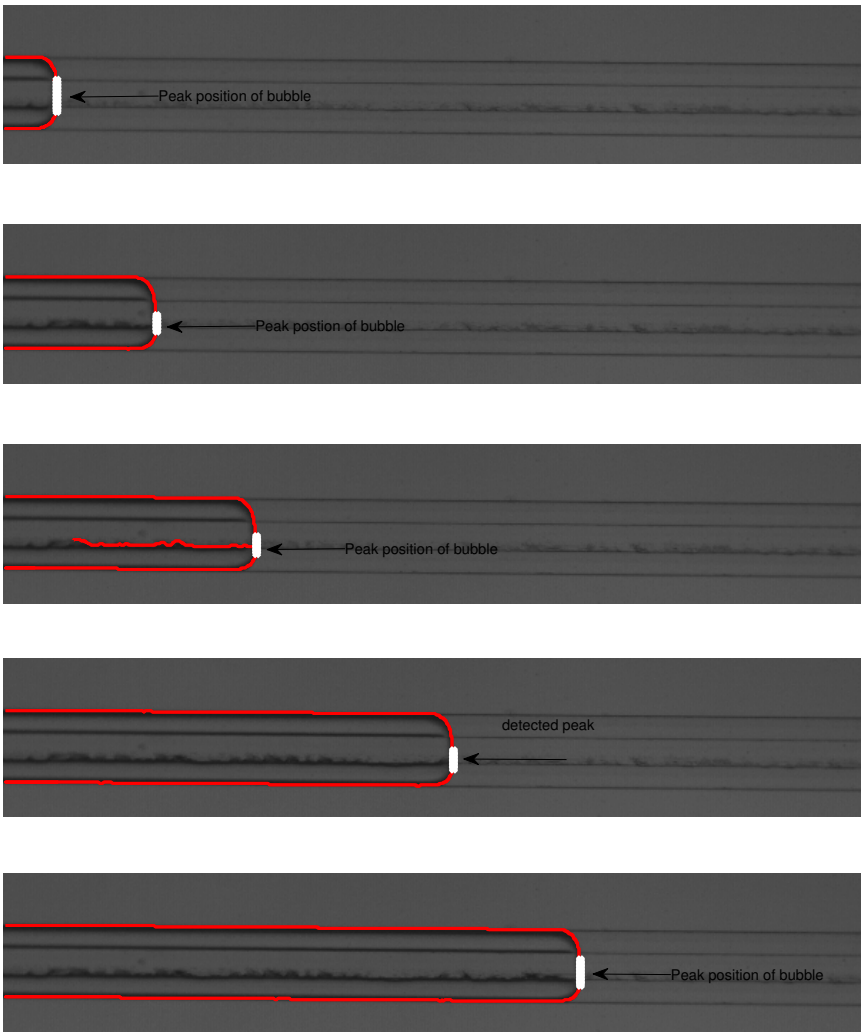

Figure 9: Matlab output of the detected peak positions of a finger as it propagates through the channel from left to right.

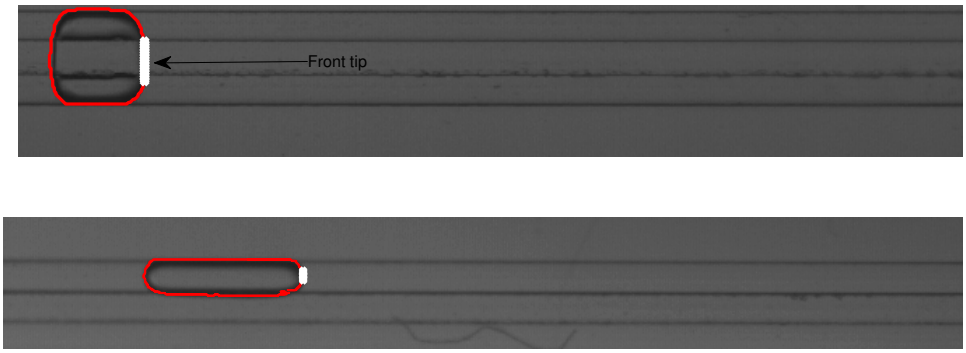

Figure 10: Matlab output of the detected front tip positions of symmetric and localized finite bubbles as they propagate through the channel from left to right.

Chapter 5

5 Experimental Results

5.1 Multiple Family of Propagating Fingers.

The morphology of an air finger/bubble as it propagates through the tube depends strongly on Ca and the obstacle dimension. In our experimental measurements, this is observed by the changes in the shape of the bubbles and also, in the measurements of the finger velocity. The nature of these fingers and their oil recovery properties is a function of a bulk measure of the fluid displacement given by the wet fraction m. Top-views of the different types of fingers and bubbles observed in our experiments are shown in figures (11 - 18). The arrows indicate the direction of motion of the finger/bubble.

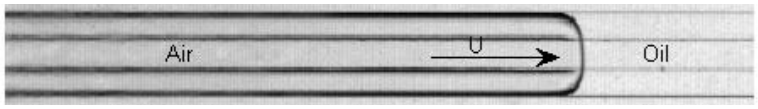

Figure 11: Symmetric finger; the arrow indicates the direction of flow in all cases. $Ca = 0.0026$ Channel 2

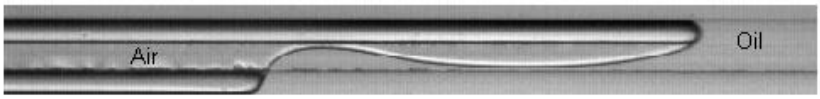

Figure 12: Asymmetric finger. $Ca = 0.014$ Channel 1

Figure 13: Localized finger. $Ca = 0.032$ Channel 3

Figure 14: Oscillatory finger. $Ca = 0.057$ Channel 2

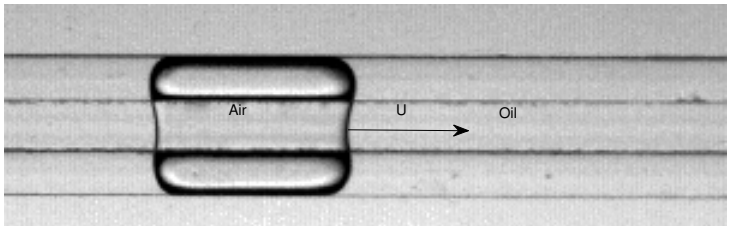

Figure 15: Symmetric finite bubble; the arrow indicates the direction of flow in all cases. $Ca = 0.0025$ Channel 3

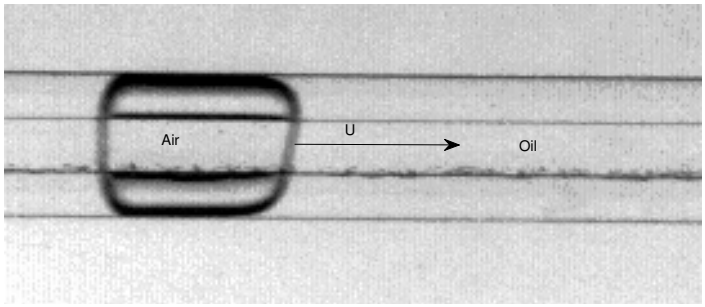

Figure 16: Asymmetric finite bubble. $Ca = 0.013$ Channel 1

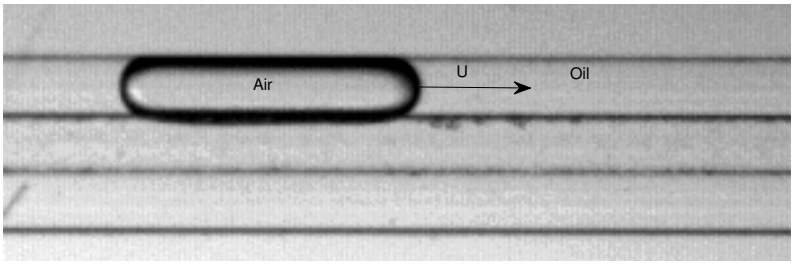

Figure 17: Localized finite bubble. $Ca = 0.047$ Channel 3

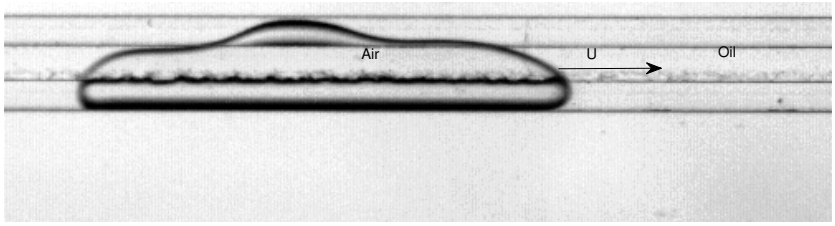

Figure 18: Oscillatory finite bubble. $Ca = 0.053$ Channel 2

The series of top-view pictures as above, clearly revealed that long and short bubbles exhibit similar propagation states.

5.2 Bifurcation graphs

We conducted severial series of experiments in the three tubes initially filled with viscous fluid and driving in air through the tubes by withdrawing the liquid at the end of each tube. The flow rate was incremented in steps of $Q = 30\ \mu l/\text{min}$. At low values of capillary number, a thin film of fluid was deposited on the tube wall behind the advancing bubble tip. As Ca is increased, which corresponds to increasing Q, a thicker film of fluid is deposited on the walls of the tubes. This is because the interface curvature increases due to increase in fluid pressure gradient that drives the axial flow. Further increment of Ca above a critical capillary number Ca_c, the symmetric bubbles lose stability to asymmetric non-localized bubbles which subsequently, localized through symmetry-breaking [19]. The localized finger selects a path of least constricted region of the tube cross-section. This is because, the minimal but unavoidable imperfaction in the manufacturing of the obstacle, introduced bias into the system. Figure 19 is a plot of a bifurcation graph of channel 1 obtained by constant increment of the flow rate in steps of $Q = 30\ \mu l/\text{min}$. The experiment was conducted at the beginning and at the end of the channel. Each data point represents a single experiment. At low capillary number, $0 < Ca \leq 0.012$, symmetric fingers propagate through the tube both at the beginning and at the end. As the capillary number increases not beyond $Ca_c = 0.012$, there is a monotonic increase in the wet fraction. Further increment of the capillary number beyond Ca_c deforms the tip of the advancing finger due to increases in fluid pressure, a feature common to many front propagating systems such as bubbles advancing in rigid tubes and Hele-Shaw channels [9, 11, 16, 17, 28]. The increase in the fluid pressure, causes the finger to lose its symmetry about the vertical midplane running parallel to the length of the tube, thereby selecting a path of least resistance and localizes at one side of the chan-

nel wall shown in the inset of figure 19. Similar scenario as in channel 1 was also observed in channel 3 as shown in figure 20. In channel 2 with lower obstacle height, we observed symmetric fingers at lower capillary numbers. As the capillary number exceeds the critical capillary value of $Ca_c = 0.032$, the axial symmetry of the finger is broken, which almost smoothly transcends to asymmetric non-localized finger in which the tip propagates with an almost constant shape and speed, but leaves behind a spatially varying periodic disturbance. Top-view images of a symmetric and oscillatory fingers are shown in the inset of figure 21. This unique but complex finger propagation mode is due to the existence of a symmetry-breaking pitchfork bifurcation between the symmetric and asymmetric steady states while [15] suggested that a global homoclinic connection gave rise to the oscillatory propagation modes.

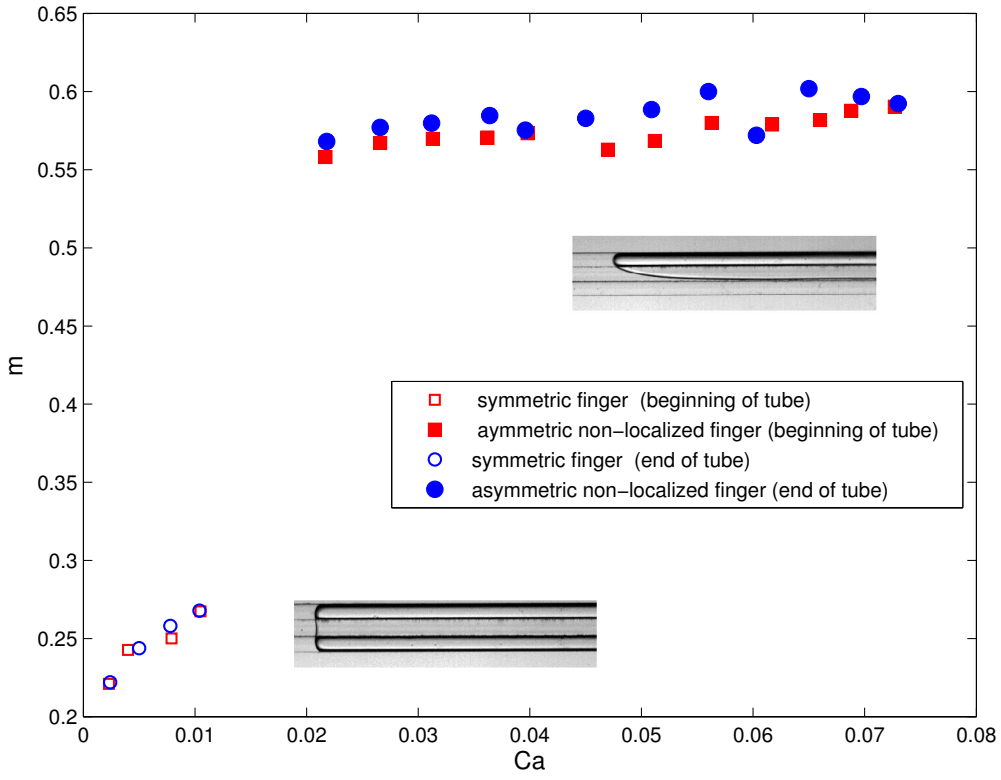

Figure 19: Channel 1: Wet fraction m as a function of capillary number Ca. The insets are top-view images of air fingers propagating through the channel from right to left. Each data point represents a single experiment. The experiment was conducted at the beginning and at the end of the channel.

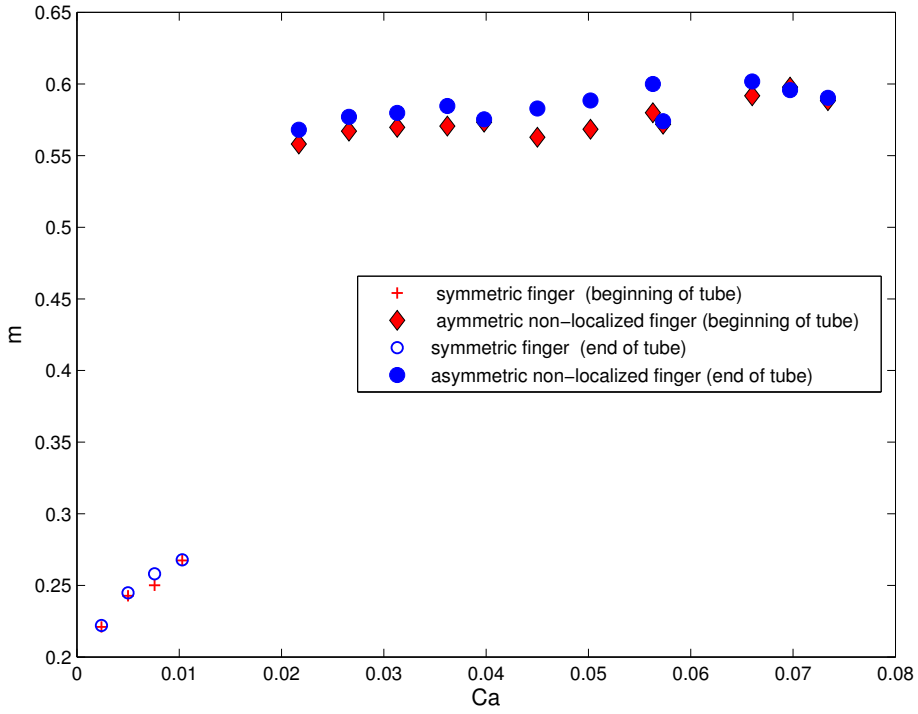

Figure 20: Channel 3: Wet fraction m as a function of capillary number Ca. Each data point represents a single experiment. The experiment was conducted at the beginning and at the end of the channel

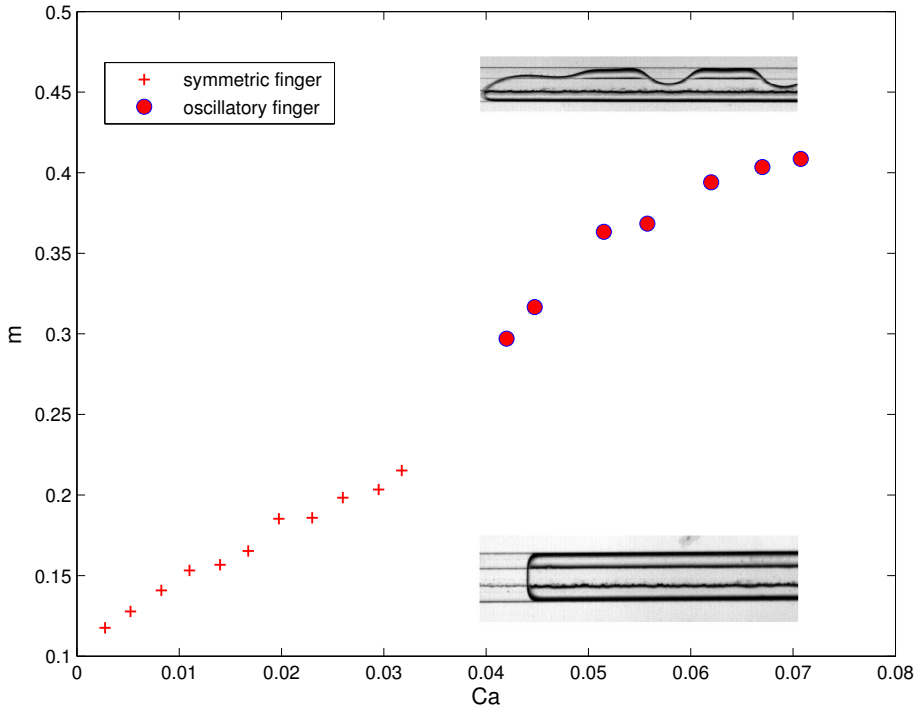

Figure 21: Channel 2: Wet fraction m as a function of capillary number Ca. The insets are top-view images of air fingers propagating through the channel from right to left. Each data point represents a single experiment conducted at the end of the channel

5.3 Oscillatory Fingers and Bubbles

Further experiments and measurements were carried out to investigate the oscillatory fingers/bubbles observed in channel 2, of which oscillatory bubbles have been shown to have applications in pumps, filters, mixers and transporters [35]. The oscillatory propagation mode is the most striking and complex feature observed in our experiments. In this context, we define 'oscillatory' to mean when the moving finger tip leaves behind a spatially varying periodic disturbance which then remains stationary in the laboratory frame. The disturbance at the interface occurs along one side of the finger, where the waves amplitudes seen are centered along the edge of the obstacle. The other side of the finger lies close to the channel wall. Consequently, the finger tip spans the region over the obstacle and one of the two unoccluded regions. Oscil-

lations emerged at high capillary numbers i.e $Ca > 0.032$. As Ca increases, there is a significant reduction in the variation of the tip shape over the period of oscilations. This mechanism for the onset of oscillations is consistent with that proposed by [15] in millimetric channels. For large-amplitude oscillations, our finger interface shapes are similar to a square wave due to the channel walls as shown in fig. 14. We noted that for air fingers, oscillations are always initiated near the finger tip and propagates backwards while finite bubbles oscillations can arise from either end of the bubble [34]. We investigate the wavelength of the finger for different flow rates as well as the finger tip length (Ltip) (define as the distance from the tip position of the finger to the point beyond which oscillation occurs) with MATLAB inbuilt 'imdistline' function. We determine the wave length by measuring the length of three consecutive fully developed wave lengths behind the Ltip and averaged it. This was done for the different images recorded for a range of flow rates with constant increment of $Q = 30$ $\mu l/\text{min}$. From our experimental results presented in figure 22, as the capillary number increases, there is rapid oil evacuation from the unoccluded region once the interface has passed over the edge of the obstacle, thereby, causing an increase in the frequency of oscillations and subsequent decrease in wavelength. This is why the wavelength decreases as Ca increases and may even cease to exist for high enough flow rates, as reported by [15] in millimetric channels. Conversely, Ltip has direct proportionality with Ca. The increase in the capillary number causes the finger to broaden more slowly across the obstacle, which induces a more rapid change in curvature; and as a result, Ltip increases with increasing Ca. See figure 23.

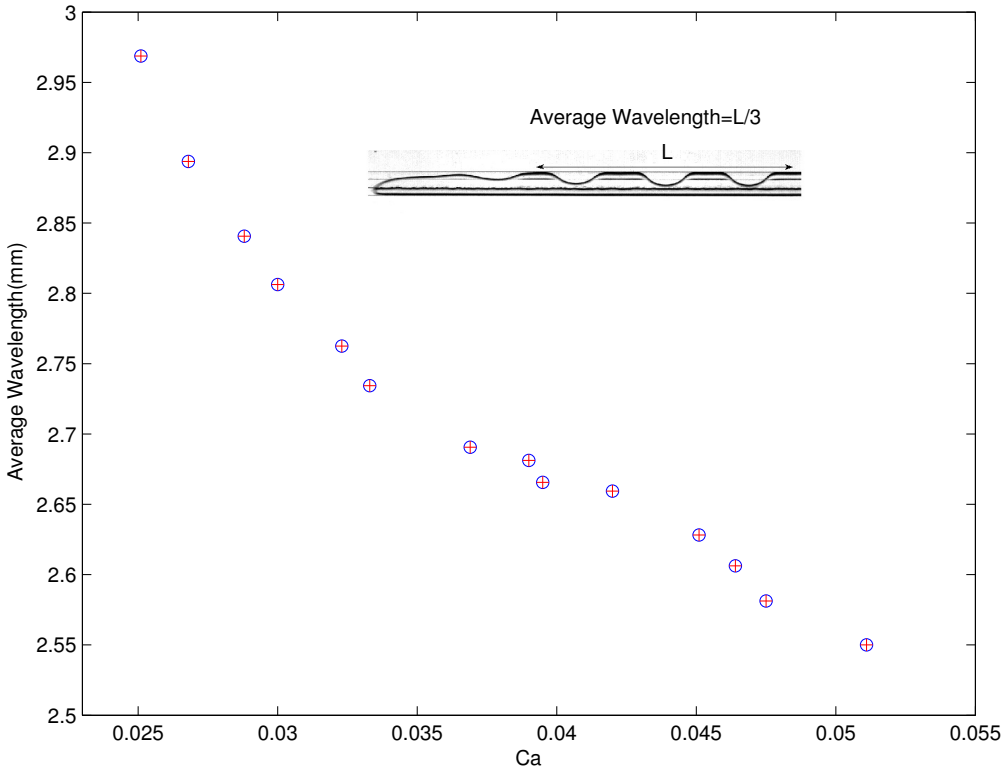

Figure 22: Characteristic wavelength (mm) obtained by averaging the length of three consecutive fully developed wave lengths behind the Ltip, ploted as a function of Ca

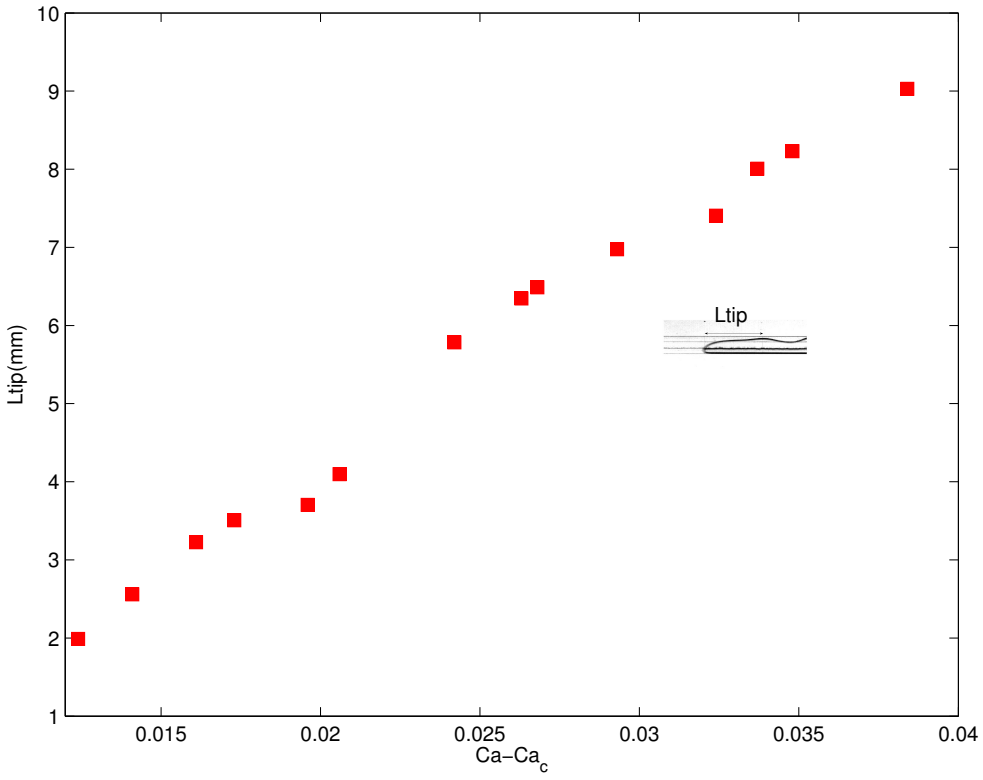

Figure 23: Characteristic tip length (Ltip) (the disdance from the tip to the position beyond which oscillations occur), plotted as a function of difference between the capillary number and the critical capillary number Ca_c. Each data point represents a single experiment.

5.4 Dynamics of finite (short) bubbles

We study the propagation of finite bubbles in tubes initially filled with fluid and investigate their bifurcation graphs to deduce if their exists any relationship between air finger and finite bubbles. Refer to §4 for the method of producing finite bubbles. We conducted the experiment with bubbles of different aspect ratios (defined as $\alpha = L/W$ where L is the distance between the front and the rear of the bubble measured in their static symmetric states and W is the width of the bubble). Each bubble was driven through the fluid filled channel by withdrawing the fluid at the end of the channel with constant increment of $Q = 30\ \mu l/\text{min}$. In fig. 24, we present the responses of finite bubbles of different aspect ratios (α) when subjected to the same flow rate. We plotted the global measure m as a function of Ca in all cases. Bubbles with $\alpha > 1$ increase monotonically and almost perfectly aligned with increase in Ca in their symmetric states and also exhibit similar pattern when in their localized states. But there is significant deviation of the data points for the bubble with $\alpha = 1$; reason we are not able to conclude at this point, but we believe there was an additional inherent drag force due to the balance between the length (L) and width (W) of the bubble. The propagation speeds of finite bubbles are generally less than that of the long fingers for the same flow rate due to the presence of a rear meniscus inducing additional drag as noted by [16] who also reported that bubbles too small to be deformed by the tube geometry, will simply act as passive tracers that will follow the flow streamlines thereby, creating a qualitative change in the flow dynamics. The inset in figure 24 is a finite bubble of $\alpha = 7/5$ when in symmetric and localized states.

Similar experiments were also conducted in channel 2 with bubbles of $\alpha = 1.3$ and $\alpha = 0.97$ and plotted on the same graph with an air finger shown in figure 25. While the air finger and the bubble with $\alpha = 1.3$ revealed obvious bifurcation point, the bubble with $\alpha = 0.97$ undergo an almost continous transition from one state to another.

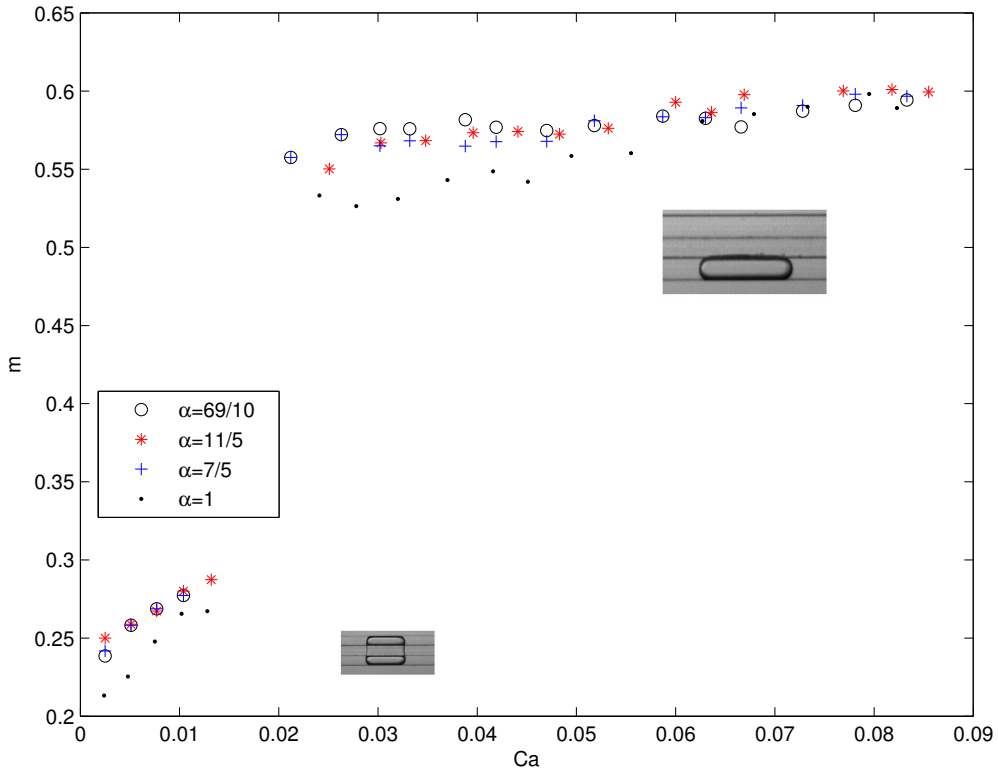

Figure 24: Channel 3: Wet fraction m as a function of capillary number Ca. We considered four bubbles with different aspect ratios as shown above. The aspect ratios are characterized as the ratio of the length and width of the bubbles measured in their symmetric static states. The insets are top-view images of a bubble with $\alpha = 7/5$ in symmetric and localized states propagating through the channel from right to left. Each data point represents a single experiment.

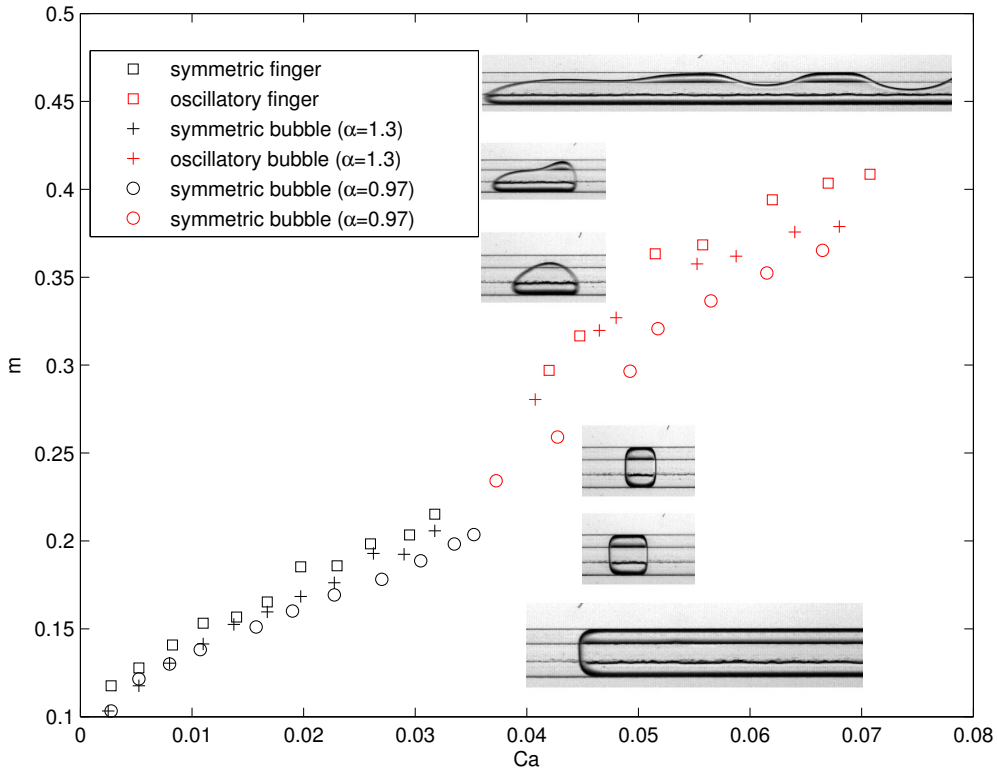

Figure 25: Channel 2: Wet fraction m as a function of capillary number Ca. The insets are top-view images of an air finger and two finite bubbles in their symmetric and oscillatory states as they propagate through the channel from left to right. Each data point represents a single experiment.

Chapter 6

6 Summary

The results of an experimental investigation of the propagation of air finger/bubble through a fluid-filled rectangular microchannel tubes with centered rectangular partial occlusion have been presented. A simple modification of the tube geometry is evident to have fundamentally altered the dynamics of bubble propagation induced by constant flux. In addition to the single, symmetric mode seen in unoccluded channels, there exists asymmetric, localized and oscillatory modes in our occluded microchannels analogous to the family of propagating fingers recently uncovered by [16, 15] in millimetre-scale tubes, indicating that gravity is not an essential physical mechanism that underpins the emergence of these states. Our results have shown that air fingers and finite bubble ($\alpha > 1$) exhibits propagation modes that are quantitatively and qualitatively similar. We observed symmetric finger/bubble at low capillary numbers which lost symmetry to either asymmetric, localized or oscillatory fingers/bubbles through supercritical symmetry-breaking bifurcation as the capillary number increases beyond a given threshold. Our results revealed almost continous transition between states for a short bubble with characteristic aspect ratio less than one. Symmetric fingers are noted for greater oil recovery property while the asymmetric, localized and oscillatory fingers limit the amount of liquid recovered. These bubble propagation modes offer further potential for geometry-induced manipulation of droplets for lab-on-chip applications.

Appendix A

MATLAB programme to detect the tip position of a finger/bubble during propagation through the channel

%Clear the work space with the command:
Clear all

% Read the reference image and save it with the variable name Im5
Im5=imread('reference image.tif');

% Similarly, read in an image of the empty channel
Im6=imread('empty.tif');

% Substract the image from the empty channel
Im=Im6-Im5;

% Crop the region of view of both the subtracted and unsubtracted images
Im=Im(30:140,200:800);
Im5C=Im5(30:140,200:800);

% Use Canny edge detection to find the edges by looking for local maxima of the gradient of Im. The gradient is calculated using the derivative of a Gaussian filter. This method uses two thresholds to detect strong and weak edges, and includes the weak edges in the output only if they are connected to strong edges.
Im=edge(Im,'Canny',a,b);

where a and b are lower and upper threshold respectively. Note: a and b are manually adjusted until a satisfactory threshold is achieved.

% View the image with the function
imshow(Im,[ ]);

% Morphologically open the binary image and remove all connected components (objects) that have fewer than P pixels, thereby, producing another binary image. We assign P =100 in our code.

Im=bwareaopen(Im,100);

% Create a flat linear structuring element that is symmetric with respect to the neighborhood center. 1 denotes the length of the line and 0 specifies the angle (in degrees) of the line as measured in a counterclockwise direction from the horizontal axis

se2=strel('line',1,0);

% Morphologically open and close the binary image Im with the structuring element se2

Imfco=imopen(Im,se2);

Imfco=imclose(Imfco, se2);

% Determine the connected components of Imfco

cc=bwconncomp(Imfco);

% Measure the properties of cc using the structure 'Area' and 'PixelList' where Area finds the number of pixels in the region while PixelList create a P-by-Q matrix specifying the locations of pixels in the region.

s = regionprops(cc, 'Area','PixelList');

% Create a vector of the binary image containing only the regions whose area is greater than 100 and find the maximum region.

idx = find([s.Area] >100);

idmax = find([s.Area] ==max([s.Area]));

```
% Find the maximum pixels locations in the region and specify their coordinates
id1=find(s(idmax).PixelList(:, 1)==max(s(idmax).PixelList(:, 1)));
id2=find(s(idmax).PixelList(:, 2)==min(s(idmax).PixelList(:, 2)));
xmax = s(idmax).PixelList(id1,1);
ymax = s(idmax).PixelList(id1,2);

% Plot the detected tip position on the original image as well as showing the image
boundary
hold on
plot(xmax,ymax,'rx');
b=bwboundaries(Im);
figure();
imshow(Im5C);
for k=1; plot(bk(:,2),bk(:,1),'r','Linewidth',2)
plot(xmax,ymax,'wx','Linewidth',3);
end
```

References

[**1**] Thorsen, T., Roberts, R. W., Arnold, F. H. and Quake, S. R. 2001, 'Dynamic pattern formation in a vesicle-generating microfluidic device' *Phys. Rev. Lett.* 86, 4163

[**2**] Dreyfus, R., Tabeling, P., and Willaime, H. 2003, 'Ordered and disordered patterns in two -phase flow in microchannels' *Phys. Rev. Lett.* 90, 144505

[**3**] Song, H., Chen, D. L., and Ismagilov, R. F. 2006, 'Droplets in microfluidic channels' *Angew. Chem. Int. Ed.* 45, 7336-7356

[**4**] Teh, S. Y., Lin, R., Hung, L. H., and Lee, A. P. 2008, 'Droplets microfluidics' *Lab-on-chip* 8, 198-220

[**5**] Baroud, C. N., and Willaime, H. 2004, 'Multiphase flows in microfluidics' *C. R. Physique.* 5, 547-555

[**6**] Sahimi, M. 1993, 'Flow phenomena in rocks: from continum models to fractals, percolation, cellular automata and simulated annealing' *Rev. Mod. Phys* 65, 1393

[**7**] Grotberg, J. B. and Jensen, O. E. 2004, 'Biofluid mechanics of flexible tubes.' *Annu. Rev. Fluid Mech* 36, 121

[**8**] Halpern, D., Fujioka, H., Takayama, S. and Grotberg, J. B. 2008. 'Liquid and surfactant delivery into the pulmonary airways' *Respir Neurobiol* 163

[**9**] Hazel, A. E. and Heil, M. 2002, 'The steady propagation of a semi-infinite bubble into a tube of elliptical or rectangular cross-section' *J. Fluid Mechanics* 470, 91-114

[**10**] Clanet, C., Herault, P. and Searby, G. 2004, 'On the motion of bubbles in vertical tubes of arbitrary Cross-sections: some complements to the Dumitrescu-Taylor problem.' *J. Fluid Mechanics* 519, 359-376

[**11**] Taylor, G. I. 1961 'Deposition of viscous fluid on the wall of a tube.' *J. Fluid Mechanics* 10, 161-165

[**12**] Whitesides, G. M. 2006, 'The origins and future of microfluidics' *Nature* 442, 368

[**13**] Hollis, C., Vahrenkamp, V., Tull, S., Mookerjee, A., Taberner, C. and Huang, Y. 2010, 'Pore system characterisation in heterogeneous carbonates: an alternative approach to widely used rock-typing methodologies. *Marine and Petroleum Geology* 27, 772-793

[**14**] Heap, A. and Juel, A. (2008), 'Anomalous bubble propagation in elastic tubes', *Physics of fluids* 20, 081702

[**15**] Pailha, M., Hazel, A. L., Glendinning, P. A. and Juel, A. 2012, 'Oscillatory bubbles induced by geometrical constraint.' *Phy. of Fluids* 24, 021702

[**16**] De Lozar, A., Heap, A., Hazel, A. L., and Juel, A.(2009). 'Tube geometry can force switchlike transition in the behaviour of propagating bubbles' *Physics of*

Fluids 21, 101702

[**17**] Hazel, A. L., Pailha, M, Cox, S. J., and Juel, A. (2013),'Multiple states of finger propagation in partially occluded tubes' *Physics of Fluids* 25, 062106

[**18**] Thompson, A. B., Juel, A. and Hazel, A. L. (2013), 'Multiple finger propagation modes in Hele-Shaw cells of variable depth.', *Journal of fluid Mechanics*(under review).

[**19**] De Lozar, A., Juel, A., and Hazel, A. L.(2008), 'The steady of propagation of an air finger into a rectangular tube', *Journal of fluid Mechanics* 614, 173-195

[**20**] Jisiou, M. (2012),'Microfluidic application of bubble oscillations induced by geometrical constraint' (Unpublished Summer Report)

[**21**] Baroud, C. N., Gallaire, F. and Dangla, R. (2010). 'Dynamics of microfluidic droplet', *Journal of the royal society of chemistry*. 10, 2032-2045.

[**22**] Fuerstman, M. J., Garstecki, P. and Whitesides, G. M. (2007) 'Coding/Decoding and Reversibility of Droplets trains in microfluidic networks', *Science*. 315, 828.

[**23**] Prakash, M. and Gershenfeld, N. (2007), 'Microfluidic bubble logic', *Science*. 315, 832.

[**24**] Link, D. R., Anna, S. L., Weitz, D. A. and Stone, H. A. (2004), 'Geometrically mediated breakup of drops in microfluidic devices', *Phys. Rev. Lett*. 92, 054503.

[**25**] De. Lozar, A., Hazel, A. L., and Juel, A. 2012, 'Scaling properties of coating flows in rectangular channels.' , *Phys. Rev. Lett*. 99, 234501.

[**26**] Juel, A. and Alexandra, H.(2007), 'The reopening of a collapsed fluid-filled elastic tube', *Journal of fluid Mechanics* 572, 287-310

[**27**] Hazel, A. E. and Heil, M. 2006, 'Finite Reynolds number effect in steady, three-dimensional airway reopening.' *Trans . ASME: J. Biomech. Engng* 128, 473-478

[**28**] Saffman, P. G. and Taylor, G. I. (1958). 'The penetration of a fluid into a porous medium or Hele-Shaw cell containing a more viscous liquid', *Proc. R. Soc. Lond*. 245, 312-329

[**29**] Hooman, F., and Masahiro, K. 2011, 'Viscous oil-water flows in a microchannel initially saturated with oil: Flow patterns and pressure drop characteristics' *Int. J. of Multiphase Flow* 37, 1147-1155

[**30**] Lichao, P., 2013, 'Complex fluids in microchannel flows at low Reynolds number: Elastic instabilities and rheology' *Ph.D Dissertation.*

[**31**] Mbanjwa, M.B., Land, K. J., Jewell, L., Moss, E. A. and Gledhill, I. M. A. 2010, 'Experimental observation of capillary instabilities of two phase flow in microfluidic T-Junction' *SACAM.* 7, 1-9

[**32**] Probstein, R. F., 1994, 'Physiochemical Hydrodynamics: An Introduction' *John Wiley & Sons,*Second edition

[**33**] Canan, C. K., 2012, 'Bifurcation analysis and its applications, Numerical Simulation-From Theory to Industry, Dr. Mykhaylo Andriychuk (Ed.), ISBN: 978-953-51-0749-1, InTech, DOI: 10.5772/50075'

[**34**] Jisiou, M., Dawson, G., Thompson, A. B., Mohr, S., Feilden, P. R., Hazel, A. L., and Juel, A. 2014, 'Geometry-induced oscillations of finite bubbles in microchannels' *Procedia IUTAM* 11, 81-88**:**

[**35**] Hashmi, A., Yu, G., Reilly-Collette, M., Heiman, G., and Xu, J. 2012, 'Oscillating bubbles: a versatile tool for lab on a chip applications.' *Lab on a Chip* 12, 4216-4227**:**